AGU ADVANCING EARTH AND SPACE SCIENCES

Water Resources Research

RESEARCH ARTICLE
10.1029/2023WR036035

Special Section:
Impacts on Water Resources of Coupled Hydrological, Chemical, and Mechanical Processes in the Fractured Subsurface

Hybrid Discrete Fracture Network Inversion of Hydraulic Tomography Data From a Fractured-Porous Field Site

Lukas Römhild[1], Lisa Maria Ringel[1], Quan Liu[2], Linwei Hu[3,4], Thomas Ptak[2], and Peter Bayer[1]

[1]Institute of Geosciences and Geography, Martin Luther University Halle-Wittenberg, Halle (Saale), Germany, [2]Faculty of Geoscience and Geography, University of Göttingen, Göttingen, Germany, [3]Institute of Geosciences, Christian Albrechts University Kiel, Kiel, Germany, [4]GeoAnalysis-Engineering GmbH, Kiel, Germany

Key Points:

- A novel inversion approach for hydraulic tomography (HT) data considering flow in both discrete fractures and porous matrix is introduced
- The method is applied to HT data from a fractured-porous field site in Göttingen (Germany)
- The results are successfully validated against independent thermal tracer test data

Supporting Information:

Supporting Information may be found in the online version of this article.

Correspondence to:

L. Römhild,
lukas.roemhild@geo.uni-halle.de

Citation:

Römhild, L., Ringel, L. M., Liu, Q., Hu, L., Ptak, T., & Bayer, P. (2024). Hybrid discrete fracture network inversion of hydraulic tomography data from a fractured-porous field site. *Water Resources Research*, *60*, e2023WR036035. https://doi.org/10.1029/2023WR036035

Received 14 AUG 2023
Accepted 5 JAN 2024

Author Contributions:

Conceptualization: Lukas Römhild, Lisa Maria Ringel, Quan Liu, Linwei Hu
Data curation: Lukas Römhild, Quan Liu, Thomas Ptak
Investigation: Lukas Römhild, Lisa Maria Ringel
Methodology: Lukas Römhild, Lisa Maria Ringel

Abstract The accurate characterization of hydraulic conductivity heterogeneities in an aquifer is crucial for predicting flow and transport processes correctly. Hydraulic tomography (HT) experiments are often used to infer the hydraulically relevant features, but the correct inversion of the data remains a challenging task. We implemented a discrete fracture network (DFN) inversion approach that is expanded by considering a nonzero matrix permeability. The hybrid model allows the accurate characterization of fractured-porous sites by taking into account both matrix and fracture flow. This novel inversion algorithm is successfully applied to HT data acquired at a field site in Goettingen (Germany), and the results are compared with those of a standard travel time inversion. Furthermore, we validate the inversion results by using them as the underlying material parameters for simulating heat tracer experiments and comparing the modeled temperature responses with those of heat tracer tests actually conducted at the site. It is shown that the DFN ensemble predicts the thermal response of the experiments correctly for the two major fractures in terms of location, amplitude, and time-dependent behavior of the temperature anomaly, as long as the stochastic nature of the results is taken into account. We conclude that considering both matrix and fracture flow in a hybrid DFN inversion approach can lead to significant improvements in flow and transport modeling at fractured-porous sites.

Plain Language Summary For understanding groundwater processes correctly, precise knowledge about the relevant geological structures in the subsurface is crucial. To infer this information, hydraulic tomography (HT) experiments are often used, which are based on sequential pumping tests in boreholes. The acquired data are usually processed by inversion techniques that allow for computing a subsurface model from the field observations. There are two different conceptual approaches: (a) continuum models, which assume a smooth distribution of the hydraulic parameters, and (b) discrete fracture network (DFN) models, which are based on an impermeable rock matrix, crossed by a limited number of fractures exclusively responsible for groundwater flow. However, certain sites show characteristics of both models, meaning that both the rock matrix and individual fractures are relevant. Therefore, we developed a new inversion technique (hybrid DFN inversion) that combines the two approaches. The method is tested on HT data acquired at a field site in Goettingen (Germany), and the results are validated against data from independent experiments (thermal tracer tests). It is shown that the subsurface models from the new hybrid DFN inversion are more accurate and reliable. We conclude that groundwater modeling at those sites can be improved significantly when using the new inversion method.

1. Introduction

The prediction of flow and transport behavior in aquifers is relevant for many applications in subsurface engineering and hydrogeology, such as geothermal energy, management of groundwater resources, and storage of hydrogen or methane (Attard et al., 2020; Gasanzade et al., 2021; Li et al., 2022). However, the accuracy and reliability of the prediction depend on the characterization of the subsurface heterogeneity. Various tomographic methods have been established for imaging the distribution of hydraulic properties. Among these methods, hydraulic tomography (HT) is based on sequentially injecting (or extracting) water in one borehole interval and monitoring the transient pressure or hydraulic head response in other nearby intervals at different depths (Yeh & Liu, 2000). The tomographical configuration created by this setup is inspired by geophysical tomography methods such as crosswell seismic or electrical resistivity tomography (Bing & Greenhalgh, 2000; Binley & Slater, 2020; Bregman et al., 1989). However, in contrast to geophysical methods, HT provides a direct link between the measured signals and the hydraulic properties of the fracture network or the porous media (Day-Lewis et al., 2017).

Project Administration: Thomas Ptak, Peter Bayer
Resources: Thomas Ptak, Peter Bayer
Software: Lukas Römhild, Lisa Maria Ringel
Supervision: Quan Liu, Linwei Hu, Peter Bayer
Visualization: Lukas Römhild
Writing – original draft: Lukas Römhild, Lisa Maria Ringel
Writing – review & editing: Quan Liu, Linwei Hu, Thomas Ptak, Peter Bayer

All pressure responses measured at the observation points can be used to invert the stratigraphic structures, that is, the spatial distribution of hydraulic diffusivity, specific storage or hydraulic conductivity.

In general, two conceptual models are available for the inversion of the hydraulic head responses: the heterogeneous continuum model and the discrete fracture network (DFN) model. The application of a continuum model results in a spatial (element-wise) distribution of hydraulic parameters. It is assumed that the heterogeneities in hydraulic parameters are attributed exclusively to matrix flow, meaning that individual (discrete) fractures cannot be inferred. The continuum model is well established for the characterization of porous and fractured sites (e.g., Berg & Illman, 2011; Cardiff et al., 2013, 2019; Fischer et al., 2017; Illman et al., 2009; Liu et al., 2022; Luo et al., 2023; Ren et al., 2021; Somogyvári & Bayer, 2017; Tiedeman & Barrash, 2020; Zha et al., 2015; Zhao et al., 2019, 2023) and several inversion methods have been developed based on this concept. While geostatistical approaches can generate tomograms for both hydraulic conductivity (K) and specific storage (S_S) and often produce the best results for drawdown predictions, continuum-based travel time inversion only yields diffusivity (D) tomograms, but allows for the accurate characterization of high-D zones with less hydraulic data being required for the inversion (H. Qiu et al., 2023). In particular, travel time inversion is considered a more efficient inversion approach in terms of computational costs and less reliance on a forward model for evaluating the error between simulated and measured data (Brauchler et al., 2003, 2013; Hu et al., 2011; Liu et al., 2022; Yang et al., 2020). Thereby, potentially insufficient initial and boundary conditions can be avoided.

Further insights into the properties of fracture networks can be gained by implementing a DFN model for the inversion. The hydraulic properties of a predefined DFN structure (Klepikova et al., 2014, 2020), the structural properties (Somogyvári et al., 2019), or structural and hydraulic properties of DFNs (Fischer et al., 2020; Ringel et al., 2022) can be estimated. Typically, the contribution of the matrix to the flow is neglected in the DFN model, but the approach can infer individual (discrete) fractures based on the HT data.

In this study, we investigate the HT-based characterization of a fractured-porous field site. This category of aquifers can be of great relevance for geothermal applications (e.g., Bauer et al., 2017; Boersma et al., 2021; Huang et al., 2021; Kushnir et al., 2018). Reliable inversion results can help to optimize the planning and operation of these sites. For that purpose, we develop a novel inversion strategy using a hybrid DFN model. It is based on a DFN inversion algorithm that has been applied for fractured crystalline rock masses assuming an impermeable rock matrix (Ringel et al., 2021, 2022; Somogyvári et al., 2017). However, at fractured-porous sites the characteristics of purely fractured rocks and a porous rock matrix with considerable permeability are combined and therefore it might not be sufficient to rely on either a continuum model or a DFN model alone. Instead, a combined (hybrid) approach considering flow in both discrete fractures and the porous matrix becomes necessary (Fischer et al., 2020). Therefore, the objective of this study is to expand the existing DFN inversion approach by the implementation of a hybrid model with a nonzero matrix permeability. We demonstrate this methodology for HT experiments conducted at the fractured rock experimental site located at the campus of the University of Göttingen, Germany, and compare the results with those obtained by using a continuum model alone.

This paper is structured as follows: subsequently, a description of the field site, the conducted HT experiments, and the fundamentals and implementations of both inversion algorithms are presented (Chapter 2). Afterward, we evaluate the inversion results in Chapter 3 and validate the results by predicting and comparing the measured data of independently conducted heat tracer tests at the field site in Chapter 4. The results are discussed in Chapter 5, where we also present a comparison between the continuum model and the hybrid DFN approach. A conclusion of our findings is given in Chapter 6.

2. Methods

2.1. Site Description and Data Acquisition

The experimental site is located at the north campus of the University of Göttingen, Germany (Figure 1a), at the eastern shoulder of the Leinetalgraben, which is a distinctive zone of subsidence in the southern part of Lower Saxony, Germany. The geological structure is complex due to polyphase tectonic development under various tension forces. Lithologically, the area is located in the Lower and Middle Keuper, which mainly consists of clay sequences and silt-sandstone layers.

The lithological situation of the site has been described in Werner (2013) based on drill cores. The top 14 m are composed of quaternary limestones and claystones with mineralizations of quartz, feldspar, and calcite. Below

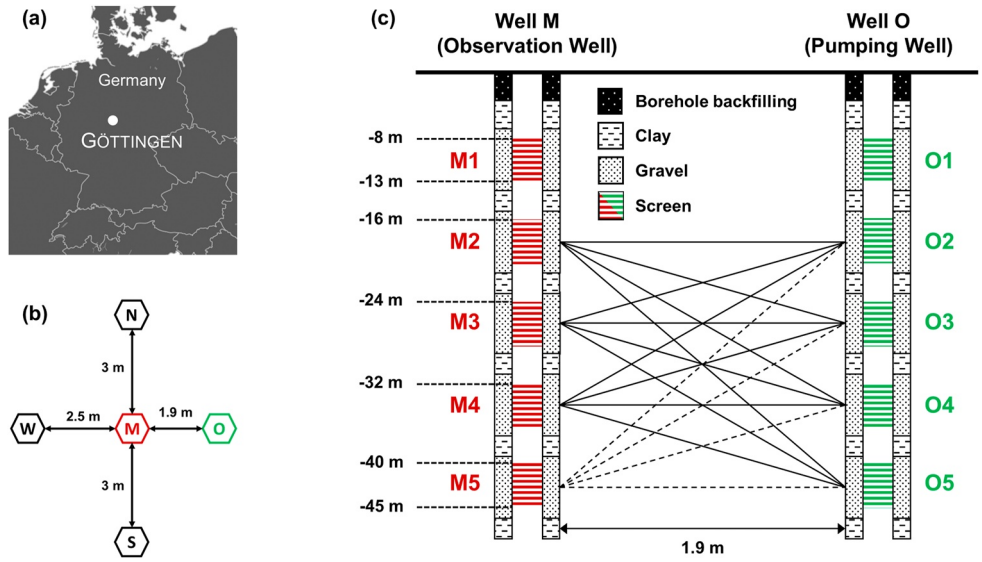

Figure 1. (a) Location of the field site in Göttingen within Central Europe. (b) Setup of the wells at the field site. (c) Tomographic configuration of the HT experiment with pumping screens in green and observation screens in red colors. The data recorded at M5 were not used due to high noise levels (dashed ray paths).

this depth, different types of consolidated sediments of the Middle Keuper can be found, starting with red and gray siltstones as well as fine sandstones between 14 and 24 m, with a high abundance of calcite mineralizations. Between 24 and 42 m, gray claystones as well as siltstones are present, again with calcite mineralizations, but also iron oxide films and small amounts of mica. An alternation of different silt- and claystones continues until 64 m depth, where the Lower Keuper begins. For more details about the geological setting and the lithology we refer to Werner (2013).

Since 2013, five groundwater wells arranged in a cross shape have been installed at this site (Figure 1b). Each well is 80 m deep and the horizontal distances from the middle well to other wells are between 1.9 and 3 m. To hydraulically connect to the surrounding strata at different depths, each well was fitted with nine separate filter sections. Each filter screen is 5 m long and installed in alternation with a 3 m impermeable filter section backfilled with clay, except for the 8 m long casing at the top of the well (Figure 1c). Therefore, tomographic pumping tests can be performed independently between different filter sections of the test and observation wells, which are hydraulically isolated by the double-packer system. Also, fiber-optic cables were pre-buried outside each wellbore in order to observe the temperature changes along the wells at high resolution during thermal tracer tests. Based on previous studies including geophysical borehole logging (Werner, 2013), flowmeter logging (Liu, 2022), long-term heat injection tests (Baetzel, 2017), and hydraulic tests (Liu et al., 2023; P. Qiu, 2020; Yang et al., 2020), the hydraulic connection between wells M and O in the upper 45 m seems most significant and several transmissive fractures can be inferred. Therefore, the cross-well area between wells M and O in the upper 45 m will be the focus of this study (Figure 1c).

The HT experiments were conducted in April 2018 as a series of cross-well multi-level pumping tests. A submersible pump (Grundfos MP1) was used to extract groundwater from isolated intervals in well O with a pumping rate of approximately 30 l min^{-1} (the exact rate for each test was recorded and could be used in the forward model of the hybrid DFN inversion). The resulting drawdown data were recorded by pressure transducers ("Druck" pressure sensors with an accuracy of 1 mmH_2O and a temporal resolution of 20 ms) in both the pumping well O and the observation well M in the intervals separated by the double packer systems. The pumping tests were conducted in four different intervals (O2-O5), and for each test the resulting pressure response was recorded in the respective four intervals (M2-M5) in the opposite borehole, thereby creating a tomographic configuration. Drawdown data were also recorded in the pumping well O, but they are strongly affected by the three-dimensional diffusion of the pressure perturbation (radially, assuming an isotropic medium), which is not included in the 2D forward model. Therefore, these data are not used within this work. Furthermore, the pressure signal at observation interval M5 is extremely noisy and was therefore excluded from the further processing and inversion (dashed

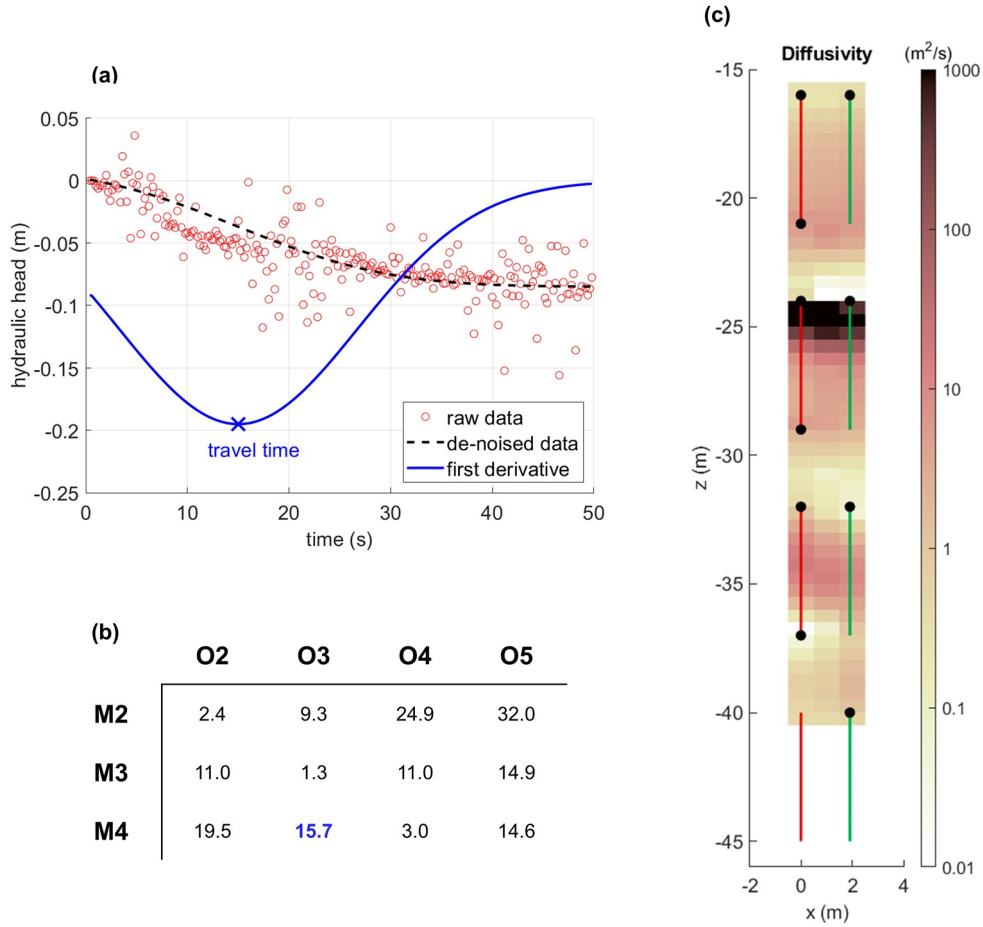

(b)

	O2	O3	O4	O5
M2	2.4	9.3	24.9	32.0
M3	11.0	1.3	11.0	14.9
M4	19.5	15.7	3.0	14.6

Figure 2. (a) Example for pressure response curves of the HT experiment and travel time processing. The raw data (red curve) are first denoised (black, dashed line), before the maximum of the first derivative (blue line) is picked as the travel time for the corresponding ray path. (b) Table with the derived travel times (in seconds) for all source-receiver combinations. The travel time from plot (a) is marked in blue. (c) Result of the travel time inversion in terms of diffusivity D. The green and red lines represent the pumping and observation intervals, respectively, whereas the black dots visualize the assumed source and receiver points for calculating the ray paths.

lines in Figure 1c). Therefore, the used data set consists of 12 different pressure response curves (red lines in Figure 4). More information about the field experiments can be found in Yang et al. (2020).

2.2. Continuum-Based Travel Time Inversion

The hydraulic travel time of a pumping test can be defined as a line integral between a source point x_1 (where the pumping-induced pressure is generated) and a receiver point x_2 (at which the resulting pressure response curves are recorded). It is assumed that the signal travels along the path ε, which minimizes the travel time based on the given distribution of diffusivity D $\left[\mathrm{m^2\ s^{-1}}\right]$ in the subsurface:

$$\sqrt{t_{\alpha,h}} = \frac{1}{\sqrt{6 f_{\alpha,h}}} \int_{x_1}^{x_2} \frac{d\varepsilon}{\sqrt{D(\varepsilon)}}, \tag{1}$$

where $t_{\alpha,h}$ $[s]$ is the hydraulic travel time and $f_{\alpha,h}$ is a conversion factor (Brauchler et al., 2003). The subscript $_h$ indicates the usage of a Heaviside source. The travel time of the signal is obtained by selecting the maximum of the absolute value of its first derivative (see Figure 2a). In order to calculate this derivative, the raw data have to be denoised to create a smooth pressure response curve. For this purpose, we employed the wavelet method and polynomial regression as reported in Yang et al. (2020). Although the duration of the experiments is relatively

long (between 300 and 3,000 s pumping duration), the travel time can typically be found within the first seconds of the signal (see Figure 2b).

Similar to the seismic travel time inversion, Equation 1 is resolved using ray tracing techniques, and the inverted slowness can be converted to the hydraulic diffusivity D. In this study, the open-source framework pyGIMLi is utilized to invert the hydraulic travel times, which is based on the generalized Gauss-Newton method (Günther et al., 2006; Rücker et al., 2017) and where the forward operator for calculating the travel times uses Dijkstra's algorithm (Dijkstra, 1959). As a final step, the diffusivity D might be converted to hydraulic conductivity K $\left[\mathrm{m\,s^{-1}}\right]$ by multiplying with specific storage S_s $\left[\mathrm{m^{-1}}\right]$:

$$K = D \cdot S_s. \tag{2}$$

The spatial distribution of S_s can be inferred from hydraulic attenuation inversion (Brauchler et al., 2011; Song et al., 2023), but it is often assumed homogeneous by using literature values. Within this study, we use a constant specific storage of $S_s = 5 \cdot 10^{-5}\ \mathrm{m^{-1}}$ based on average values from P. Qiu (2020).

For performing the inversion, a uniform rectangular grid with a vertical resolution of 0.5 m and a horizontal resolution of 1 m is used. The relatively coarse resolution is chosen to account for the low data density produced by the limited number of source and receiver positions. The model space using this grid consists of 150 cell values, while the data space is made up by only 12 travel times. Therefore, an even finer resolution would pretend an accuracy of the result that is not actually supported by the data. Furthermore, the rectangular (non-square) cells are helpful to reproduce the horizontal layering typical for sedimentary environments, without the need to apply anisotropic constraints within the inversion. While the pumping and observation intervals have a relatively long vertical extension (red and green lines in Figure 2c), the source and receiver positions are only modeled as points that are set at the top or bottom of the interval (black dots in Figure 2c). Since the travel time inversion is generally most sensitive to the shortest path of the signal, the receiver points are placed at the position that minimizes the distance to the respective pumping location. Consequently, since results from a travel time inversion can only cover the domain between source and receiver points, no diffusivity information can be obtained for the area between the deepest intervals (−40 to −45 m), as well as beyond the pumping and observation locations in horizontal direction.

2.3. Hybrid DFN Inversion

2.3.1. Forward Simulation and Numerical Model

Since the HT data were acquired at a fractured-porous field site, a hybrid DFN model, also called discrete fracture matrix (DFM) model, is applied for the simulation of the HT experiments (Berre et al., 2019). This conceptual model integrates larger and more permeable fractures directly while smaller and less conductive fractures are considered by the hydraulic conductivity and specific storage of the matrix elements. Flow in the fracture network and the porous media is governed by Darcy's law and the continuity equation. The porous medium is modeled as 2D continuum:

$$S_s \frac{\partial h}{\partial t} - \nabla(K \cdot \nabla h) = Q \tag{3}$$

with the following initial and boundary conditions:

$$h\,|_{t=0} = 0, \quad h\,|_{\Gamma_1} = 0, \quad (K \cdot \nabla h) \cdot \mathbf{n}\,|_{\Gamma_2} = 0. \tag{4}$$

Here, h [m] is the hydraulic head, Q $\left[\mathrm{s^{-1}}\right]$ is a source/sink term, Γ_1 comprises the left and right boundary of the domain, Γ_2 the top and bottom boundary, and $\mathbf{n}$ is a normal vector on the respective boundary.

Fractures are reduced to 1D discrete lines assuming a constant hydraulic head normal to the fracture plane:

$$a_f\, S_{s,f} \frac{\partial h}{\partial t} - \nabla_T(a_f\, K_f\, \nabla_T h) = a_f\, Q, \tag{5}$$

where a_f [m] is the fracture aperture. The gradient ∇_T is evaluated in the fracture plane. The subscript $_f$ always refers to fracture parameters (in contrast to porous media parameters).

Table 1
Minimum and Maximum Values for the Prior Distribution of Fracture Parameters

Parameter	Minimum	Maximum
x-position of the fractures mid-point	−8 m	10 m
z-position of the fractures mid-point	−46 m	−15 m
Length of the fracture	0.5 m	10 m
Hydraulic conductivity of the fracture	10^{-4} m s^{-1}	10^{0} m s^{-1}

The finite element method (FEM) is applied for the numerical solution of Equations 3 and 5. Intersections between different fractures and between fracture and matrix are considered by a conforming mesh discretization which imposes continuity of the head and balance of the fluxes (Woodbury & Zhang, 2001). The mesh discretization for the computational domain including the boreholes and the fracture network is implemented utilizing the open source mesh generator *Gmsh* (Geuzaine & Remacle, 2009).

2.3.2. Solution of the Inverse Problem

The inversion of the HT data is based on a stochastic approach. Accordingly, the DFN parameters θ (a parameter set containing position, size, and hydraulic conductivity K of the fractures, see Table 1) are interpreted as random variables characterized by their posterior distribution $p(\theta|\mathbf{d})$. The Bayesian equation relates the posterior distribution, considering a set of measured HT data, to the likelihood of the modeled data for a given DFN realization and the prior information of the DFN parameters. The likelihood function L evaluates the error between the measured HT data $\mathbf{d}$ and the HT signals $\mathbf{f}(\theta)$ simulated by the forward model:

$$\log\ L(\mathbf{d}|\theta) \propto -\sum_{i=1}^{N_{\text{data}}} \frac{(d_i - f(\theta)_i)^2}{2\sigma_i^2}, \tag{6}$$

where $\boldsymbol{\sigma}$ is the data variance estimated by Gibbs sampling, as in previous works (Ringel et al., 2019, 2022). The posterior distribution of the DFN parameters is evaluated by generating samples from the distribution according to Markov chain Monte Carlo (MCMC) methods. This results in a set of DFN realizations that are equally likely by adjusting the structural and hydraulic properties of the DFN. Starting from an initial DFN realization, the DFN parameters are updated iteratively by proposing a new parameter set θ' with a proposal distribution q based on the current realization of the DFN. This parameter set is accepted or rejected according to the update probability:

$$\alpha = \min\left(1, \frac{p(\theta'|\mathbf{d})}{p(\theta_{i-1}|\mathbf{d})} \frac{q(\theta_{i-1}|\theta')}{q(\theta'|\theta_{i-1})}\right). \tag{7}$$

Insertion or deletion of a fracture is a so-called transdimensional update following the reversible jump MCMC algorithm (Green, 1995). Additionally, parameter updates can be applied that adjust position, length, or hydraulic conductivity of the fractures. More information about this DFN inversion approach can be found in Ringel et al. (2022).

2.3.3. Implementation of the Inversion

The computational domain comprises a rectangle covering the depth range between 0 and −60 m in vertical (z-) direction and a horizontal (x-) extension between −10 and 12 m. The two boreholes are located at $x = 0$ m and $x = 1.9$ m, so that the distance between both boreholes and the corresponding boundary of the domain is approximately 10 m. This distance ensures that boundary effects of the model directly affecting the relevant hydraulic signals are negligible, but long fractures are still able to connect the boundary conditions with the boreholes to simulate the interaction with the parts of the aquifer not included in the computational domain. As shown in Equation 4, these boundary conditions on the left and right side of the domain were implemented as zero head boundaries due to the negligible natural flow conditions at the site. At the top and bottom of the domain, no-flow boundary conditions are employed. The initial hydraulic head is set to zero within the whole domain.

The pumping intervals are implemented as 1D line source elements using the exact vertical extension according to the field experiments (Figure 1c). The resulting pressure response curves are achieved by integrating over the volume of the borehole intervals (using the exact borehole radius and vertical extension), so that the contributions of all fractures crossing the respecting intervals, as well as the matrix, are considered.

The pumping duration and extraction rates of the individual hydraulic tests are implemented according to the actual field experiment. However, only the first 100 s of the signals were evaluated within the inversion. This early time span is the most dynamic part of the response and contains almost all necessary information about the subsurface hydraulic parameters (e.g., Hou et al., 2023). Also, using the complete signal for the inversion procedure would significantly increase the computational cost.

For modeling flow in the porous medium, we assign a hydraulic conductivity of 10^{-6} m s^{-1} and a specific storage of $5 \cdot 10^{-5}$ m^{-1} to the matrix. These values are based on earlier results of single-well multi-level pumping tests and corresponding type curve analysis, which give a range of possible values for both parameters (e.g., between $3.4 \cdot 10^{-7}$ and $1.3 \cdot 10^{-6}$ m s^{-1} for K, based on P. Qiu (2020)). A more detailed discussion of the selected matrix parameters in contained in Section 3.4.

The inversion algorithm works with a limited number of distinct fracture sets that are each characterized by a fixed fracture orientation angle. Based on data from an optic televiewer system, three major orientations of the fractures were identified by an earlier study (Werner, 2013) in terms of azimuth and dip angle: 351°/6°, 221°/37°, and 45°/59°. By projecting these planes into our 2D domain, we obtain the following dip angles: −0.94°, −26.31°, and 49.64°.

At the beginning of the inversion process, an initial DFN has to be defined as the starting model. While some of the initial fractures are manually inserted to ensure connectivity to the boundary conditions, as well as between the pumping and observation intervals for the first iteration, a number of randomly generated fractures is also added. All of the initial fractures belong to one of the three fracture sets mentioned above, meaning that the orientation angles of the initial DFN are based on the three different angles from the televiewer data (Werner, 2013), and they remain fixed throughout the inversion process. Each orientation is chosen with a probability of $\frac{1}{3}$ when generating the initial DFN, and also when inserting a new fracture during the inversion process.

To evaluate the influence of the starting model, we performed several inversions with different initial DFNs in parallel. It could be observed that all inversions end up at similar posterior DFN ensembles despite large differences in the starting model. In all cases, none of the initial fractures remains untouched by the inversion. Instead, most of the direct interval connections are actually deleted and replaced by more indirect connections by a combination of several fractures. A lot of other initial fractures undergo significant changes in position and size during the inversion procedure.

All fractures in the model are assumed to be straight lines characterized by an aperture of 0.002 m (Liu et al., 2022) and a specific storage of 10^{-5} m^{-1}. While those two parameters remain fixed during the inversion, the hydraulic conductivity K as well as location and length of the fractures are regarded as inversion parameters. The minimum and maximum values used for the prior distribution of those parameters are summarized in Table 1.

Note that hydraulic conductivity is assumed to be constant within each individual fracture. The minimum and maximum number of fractures for a DFN are set to 20 and 200, respectively, while the latter has never been reached during the inversion process. The prior distributions also apply as proposal functions for the insertion of a fracture. For the deletion of a fracture, one fracture is randomly chosen from a uniform distribution over the number of fractures. In the case of a parameter update, the proposal distribution is a normal perturbation of the current value with a given standard deviation.

3. Inversion Results

3.1. Travel Time Inversion Result

The result from the continuum-based travel time inversion of the HT data is shown in Figure 2c. The tomogram is evaluated in terms of diffusivity D, since this parameter is the direct result of the inversion and no conversion to hydraulic conductivity (Equation 2) has been performed at this stage. In the result, most areas have diffusivity values between 0.1 and 10 m^2 s^{-1}. However, there is one distinct high-diffusivity zone at the depth of −25 m that connects the intervals M3 and O3. Clearly, a strong hydraulic connectivity was established between those intervals. However, the exact depth of this connection remains unclear. The inversion algorithm places the high-diffusivity zone at the top of the interval, since the source and receiver points were placed there in the forward model. In the field experiments, the complete intervals function as sources and receivers, so the connection could also be located at the bottom of these intervals (e.g., around −28 m). Therefore, it is not possible to derive the exact depth of the hydraulically relevant features using the continuum-based travel time inversion in combination with this specific field setup.

3.2. Hybrid DFN Inversion Results: Individual Realizations

First, we show the DFN realization of the last iteration as one example of the posterior ensemble in Figure 3a. This network consists of 23 individual fractures, with three of them being part of the first fracture set (dip angle

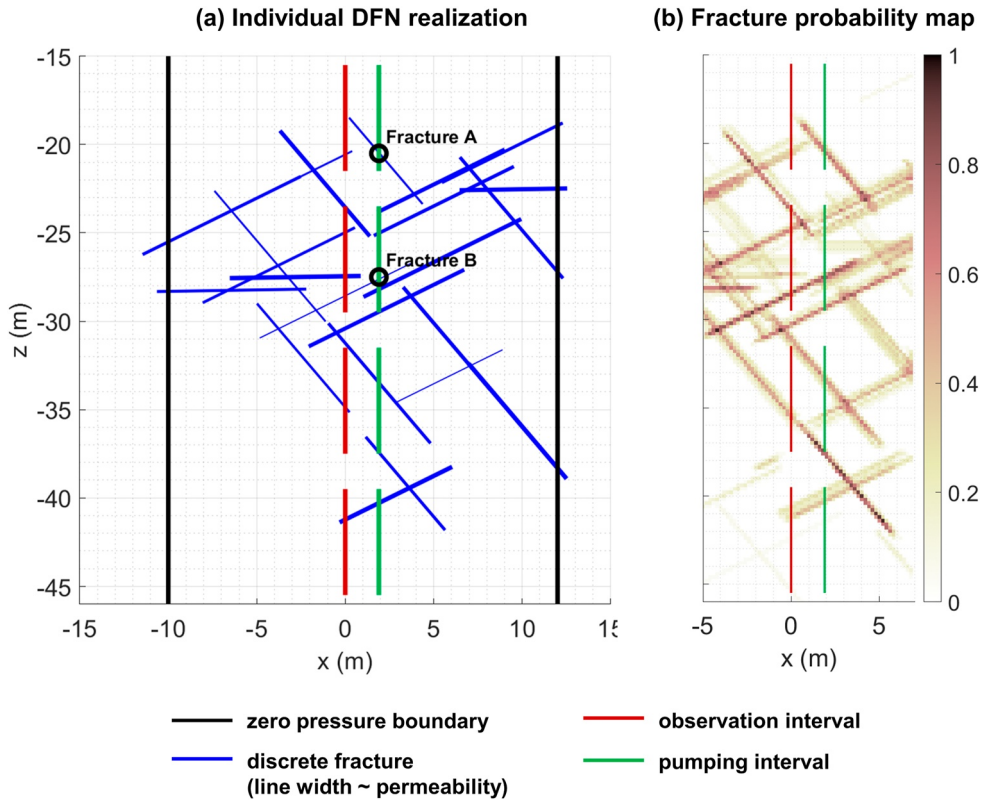

Figure 3. (a) Individual DFN realization from the last iteration of the inversion. The black lines represent the zero pressure boundary conditions (the no-flow boundaries at the top and bottom are not shown here), while green and red lines are pumping and observation intervals, respectively. The blue lines visualize the individual fractures of the DFN with the width of the line indicating the individual permeabilities. (b) Fracture probability map generated from the posterior ensemble of the hybrid DFN inversion.

−0.94°, almost horizontal lines in the plot), 11 of the second fracture set (−26.31°) and nine of the third fracture set (49.64°). The hydraulic conductivity of the fractures is visualized by the width of the blue lines and ranges from 0.25 to 0.99 m s^{-1}. All these values are close to the upper limit for K used within the inversion (1 m s^{-1}), so that even the relatively thin lines in the plot are fractures with a hydraulic conductivity significantly higher (around five orders of magnitude) than the matrix.

All fractures of this realization have a connection to the entirety of the network, either by other fractures or by the two boreholes. There are two fractures that connect the network to the left boundary and four fractures establish the connection to the right boundary (black lines). Only one direct connection between two opposite intervals can be found (marked as fracture B in Figure 3a), which corresponds with the high-diffusivity zone identified in the travel time inversion result (Figure 2c). However, many more connections between other intervals (also in vertical direction) are established in indirect ways by the interplay of several fractures. In some cases, fractures end very closely to one of the intervals, leaving a little gap, where the hydraulic connection is maintained by flow through the matrix (e.g., fracture A is very close to the pumping interval, but still leaves a small gap). In these cases, the combined fractured-porous approach is of great importance.

A comparison of the measured HT data with the modeled data based on the last DFN realization is shown in Figure 4. Overall, a good data fit has been reached for the first 100 s of the signal. The hydraulic head toward steady-state conditions has mostly been simulated correctly with values between −0.1 and −0.15 m. Only for combination O2-M4, the misfit between measured and simulated data at the last shown time step is significant. In other cases, the slope of the simulated curves is not entirely correct (e.g., combination O3-M3, where the drop in hydraulic head is actually much slower, but in the end, the same steady-state level is reached). This could be explained by an underestimation of the specific storage in either the matrix or the fracture network by the inversion but might also be a result of possible 3D effects in the experiment that are not accounted for in the

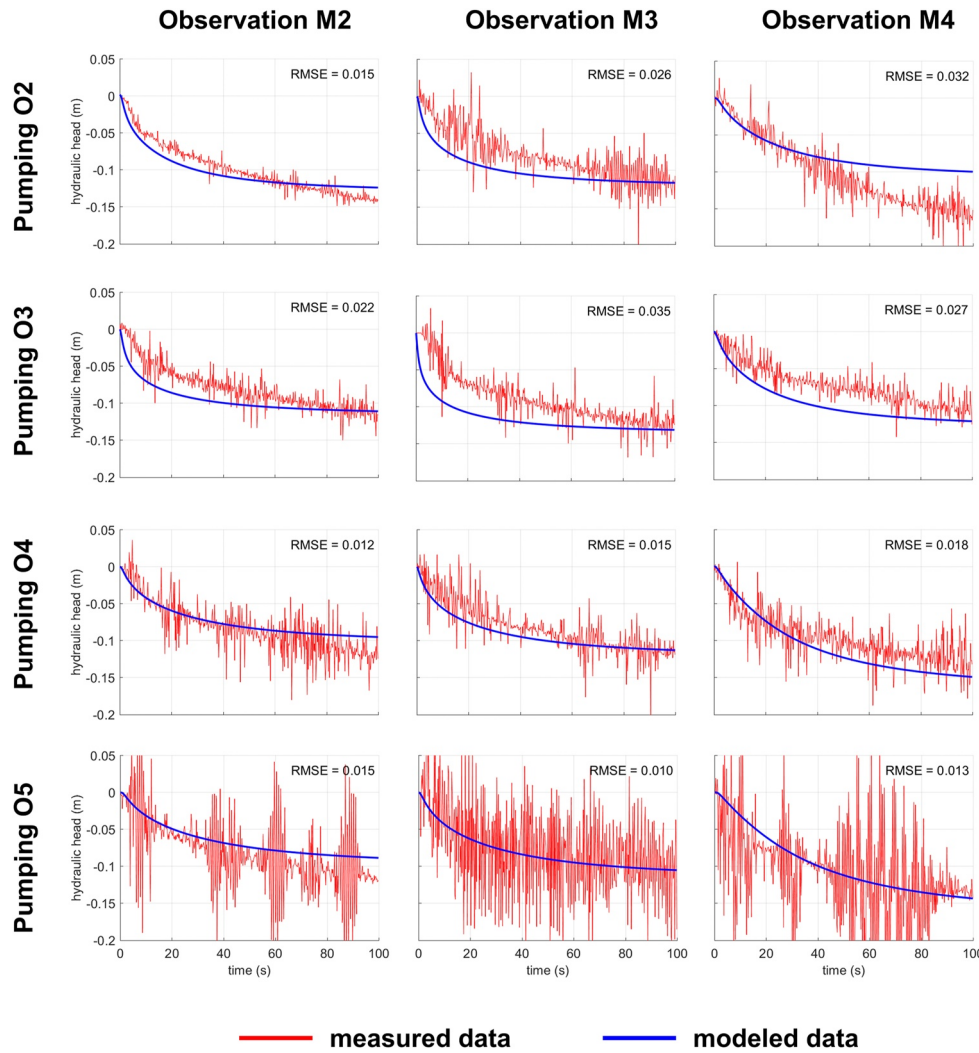

Figure 4. Measured (raw) data of the HT experiments (red lines) and modeled pressure response curves for the last iteration of the hybrid DFN inversion (blue lines). Only the first 100 s of the signal are used within the inversion procedure. The RMSE values (in m) shown in the plots are calculated using smoothed pressure response curves to eliminate the effect of noise on the RMSE. However, within the inversion procedure, the raw signal is used to include the uncertainty of the data.

2D forward model. However, with respect to the high noise level of the measured data, the simulated pressure response curves can be regarded as satisfactory.

3.3. Hybrid DFN Inversion Results: Fracture Probability Map

The high number of DFN realizations (samples from the posterior ensemble) requires the evaluation of the inversion result as a fracture probability map (FPM). Due to the large ensemble size and the strong similarity of consecutive realizations, the method of sequence thinning (Somogyvári et al., 2017) was used to select realizations that show significant differences. We use every 100th realization of the last 2,500 iterations of the ensemble. A raster with 0.2 m resolution is generated for each DFN realization and the values 1 and 0 are assigned to the individual raster elements, based on whether a fracture is present or not. By computing the mean of all rasters for the chosen DFNs, the FPM is created, showing the probability (between 0 and 1) for each raster element to be part of a fracture. The variations in hydraulic conductivity among the different fractures are not considered in the FPM.

Figure 3b shows the resulting FPM. The individual realization from Figure 3a can clearly be identified in the FPM as well, and deviations within the posterior ensemble are relatively minor. There is a limited number of

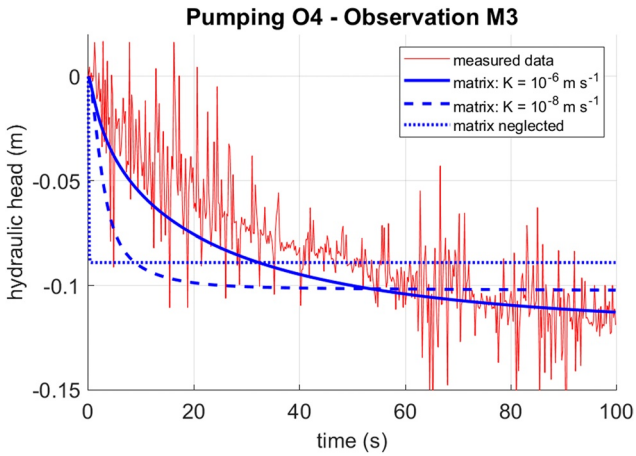

Figure 5. Influence of matrix parameters on the inversion results. Choosing a hydraulic conductivity of 10^{-6} m s^{-1} for the matrix results in the smallest misfit (solid, blue line), for example, compared to a lower *K*-value of 10^{-8} m s^{-1} (dashed, blue line), and especially compared to a classical DFN inversion neglecting the matrix completely (dotted, blue line). For the complete results of all source receiver combinations, we refer to Figures S1 and S2 in Supporting Information S1.

fractures that only appear in some realizations (e.g., in the lower left corner). Instead, most of the fractures only undergo small positional changes (blurry areas in the FPM) or are almost not being shifted at all (dark lines in the FPM). All of those fractures are in some way connected to pumping/observation intervals or to the boundary, so that they are hydraulically relevant and therefore crucial to fit the data properly.

A zone with a particularly high fracture density can be identified around the second pair of intervals (between −22 and −30 m, approximately). Here, the fracture network establishes a strong hydraulic connectivity between the opposite intervals and beyond (to the boundary). Again, fracture B appears as a very prominent feature that directly connects the intervals and is characterized by very high probabilities (dark colors) in the FPM. This zone of high fracture densities is in good agreement with the continuum-based inversion result (Figure 2c) that indicates a high-diffusivity zone in a similar depth range. Above and below these depths, a lower fracture density can be observed, with only a few distinct fractures being hydraulically relevant. Outside the area covered by the intervals, no fractures are being inserted by the inversion algorithm due to the absence of hydraulic data.

3.4. Influence of Matrix Characteristics

Within the hybrid DFN inversion approach, selecting the correct hydraulic conductivity of the matrix plays a key role. As stated previously in Section 2.3.3, we assign a hydraulic conductivity of 10^{-6} m s^{-1} to the matrix based on earlier findings of P. Qiu (2020). Generally, fitting some of the data by analytical solutions can help to find a good initial guess for the matrix parameters.

However, alternative matrix characteristics were also tested to evaluate their influence on the inversion results. If, on the one hand, the value for matrix-*K* is chosen too high, flow in the porous phase alone might explain the measured hydraulic data and therefore almost no fractures are inserted by the inversion algorithm. In this case, the matrix hydraulic conductivity is already an average value that contains both the porous and the fractured part. If, on the other hand, *K* of the matrix is chosen smaller, seemingly reasonable DFNs are generated by the inversion, but the experimental data cannot be fitted with the same accuracy. This trend is illustrated by Figure 5: When selecting a lower hydraulic conductivity of $K = 10^{-8}$ m s^{-1} for the matrix, we observe a modeled pressure response that is too rapid for explaining the measured data (dashed, blue line in Figure 5). Overall, this DFN ensemble produced higher RMSE-values between measured and modeled data and is therefore characterized by a lower likelihood compared to the original matrix-*K* of 10^{-6} m s^{-1}. The complete inversion results for all source receiver combinations are shown in Figure S1 of Supporting Information S1. It shall be noted that for both cases the misfit between measured and modeled data had remained almost constant for several thousands of iterations. It is thereby ensured that a stationary level had been reached and no better fit is possible, meaning that the shown DFN realization must be part of the posterior ensemble.

When neglecting the matrix completely (dotted, blue line in Figure 5), the modeled pressure response is even more rapid, and no satisfactory fit of the data can be achieved. The full result of this inversion case is shown in Figure S2 of Supporting Information S1. As a consequence, a classical DFN inversion cannot be suitable for this data set. Instead, the hybrid DFN inversion approach is necessary for processing the experimental data of this site, and probably also beneficial at other fractured-porous field sites.

4. Validation With Thermal Tracer Test Data

4.1. Field Experiments

The thermal experiments used for the validation are conducted in opposite direction compared to the HT experiments (Figure 1c) with heat injection in borehole M and observation of the resulting temperature response in borehole O. We evaluate the results for three different heat injections in the intervals M2, M3 and M4. The

temperature of the injected water was approximately 20°C, while the ambient temperature was around 9°C during the experiments. The tests ran for 5 hr with an injection rate of 25 l min^{-1}. In the observation well, temperatures were recorded using a distributed temperature sensing (DTS) system with a vertical resolution of 0.5 m and an observation frequency of 1 min. During each thermal tracer test, double-packer systems were installed at different filter sections in the injection well attempting to reveal fractures at different filter sections. The results of these experiments have been published previously in Liu et al. (2022).

4.2. Simulation of the Field Experiments

The thermal tracer experiments were simulated in COMSOL 6.1 (Comsol, 1998) using the different inversion results obtained from the HT experiments as the underlying representation of the hydraulic properties. The computational domain is a 60 m × 60 m 2D rectangle with no-flow boundaries at the top and bottom and zero-pressure boundaries on the left and right, similar to the model used for the hybrid DFN inversion. We found that a larger horizontal distance between the boundary conditions and the boreholes (compared to the hybrid DFN inversion) is necessary due to the longer duration of the experiments.

The travel time inversion result was first converted from diffusivity D to permeability k (Equations 2 and 8) by assuming a homogeneous specific storage of $5 \cdot 10^{-5}$ m^{-1} (the same value was used for the matrix in the DFN inversion). The resulting k-distribution was imported as a pixel map, while the rest of the computational domain outside the inversion result was filled with a constant value of $k = 1.33 \cdot 10^{-13}$ m^2, which corresponds with the value of matrix permeability within the hybrid DFN inversion ($K = 10^{-6}$ m s^{-1}) by using the conversion

$$k = \frac{\eta}{d \cdot g} \cdot K \approx 1.33 \cdot 10^{-7} \cdot K, \tag{8}$$

where η and d are dynamic viscosity and density of water, respectively, and g is the gravitational acceleration. To use the DFN result within the numerical model, several realizations of the posterior ensemble have to be implemented due to the stochastic nature of the inversion. Again, the sequence thinning method is employed to select every 100th realization of the last 900 iterations of the ensemble, meaning that the thermal tracer test simulations were conducted on 10 different DFN models. Each fracture was added manually to the numerical model as a line segment with the exact coordinates and permeability values from the inversion result. The permeability of the matrix was again assigned with $1.33 \cdot 10^{-13}$ m^2. Furthermore, porosity values of 0.3 for the matrix and 0.8 inside the fractures were assumed, as well as an average rock density of 2,700 kg m^{-3} (Schön, 2015). The thermal conductivity (0.58 W m^{-1} K^{-1} for the fluid and 3.0 W m^{-1} K^{-1} for the matrix), as well as the specific heat capacity (4,200 J kg^{-1} K^{-1} for the fluid and 1,000 J kg^{-1} K^{-1} for the matrix) are based on literature values for sandstone (Schön, 2015).

Similar to the hydraulic forward models used within the inversion procedures, a 2D model is also employed for the thermal simulations. This approximation is typically reasonable in local zones with clearly defined principal stress directions (Lang et al., 2018), which is fulfilled in this specific field case due to the small distance between the boreholes (1.9 m) and the given orientation angles of the fractures.

For all the simulations, a homogeneous temperature field of 10°C was used as initial condition and the temperature at the boundaries is kept at this value, accounting for the temperature of water inflow from the sides. In the injection interval, a mass flux of 25 l min^{-1} with a temperature of 20°C was employed, in accordance with the actual field survey. The complete time span of the experiment (5 hr) was simulated. Figure 6 illustrates the thermal tracer test simulation for one DFN realization for the injection interval M3 at three different time steps.

4.3. Comparison Between Measured and Predicted Thermal Response

Figure 7 compares the measured thermal response (left column of plots) produced by the three different injections in the intervals M2, M3, and M4 with the modeled thermal response using the continuum-based inversion result (middle column) and the hybrid DFN inversion result (right column). The results were evaluated in terms of temperature deviation ΔT from the respective minimum values since the actual temperature of the aquifer was often slightly smaller (1–2 K) than the 10°C assumed in the numerical model.

The measured data reveal two significant temperature anomalies: one for the first injection in interval M2 at a depth of −20 m with a temperature amplitude of up to 5 K, and another one for the second injection in interval

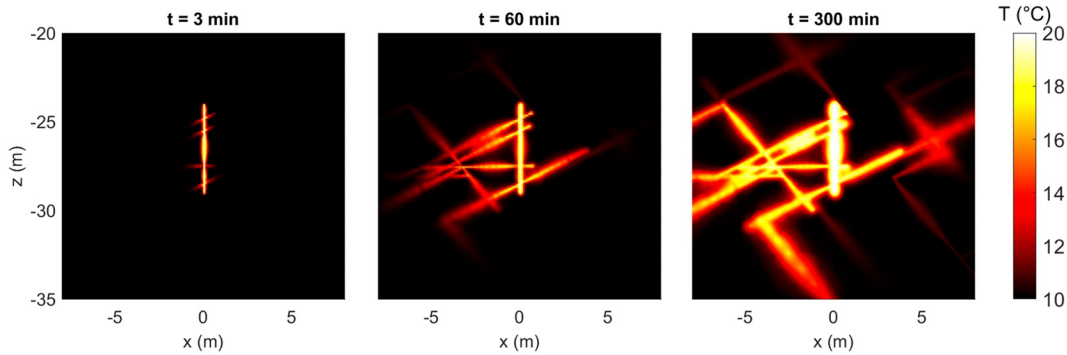

Figure 6. Snapshots of the thermal tracer test simulations performed in COMSOL for injection interval M3 at the first time step (left), after 1 hr (center) and at the last time step (right).

M3 at a depth of −28 m with a temperature amplitude of up to 8 K. We interpret these major pathways for heat transport as the two prominent fractures A and B, which can also be identified in the hybrid DFN inversion result (Figure 3a). The time-dependent behavior of the temperature breakthrough in those two fractures is also shown in Figure 8 by the red lines. In these plots, the depth with the highest temperature amplitude was used for the evaluation, as this was assumed to be the crossing point of the fracture with the observation borehole.

The other temperature anomalies with much smaller amplitude, but wider vertical extensions (red areas in the plot) are most likely a result of vertical heat transport inside the observation borehole and/or remaining heat from the respective earlier injections (the experiments were conducted from top to bottom). Both of these effects are not accounted for in the numerical model, so that the anomalies cannot be observed in the simulated data.

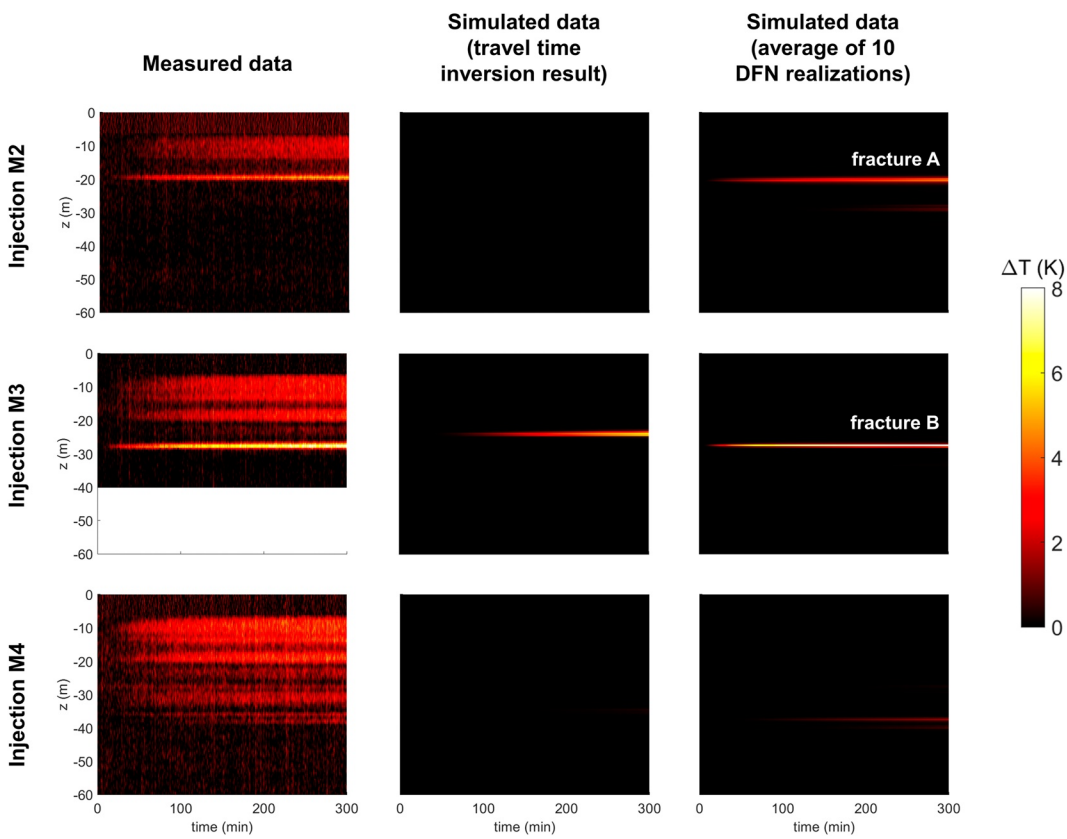

Figure 7. Comparison of measured data from the thermal tracer test (left column) and the simulated data using the travel time inversion result (center column) and the hybrid DFN inversion result (right column). Fracture A and fracture B are also shown in Figure 3a.

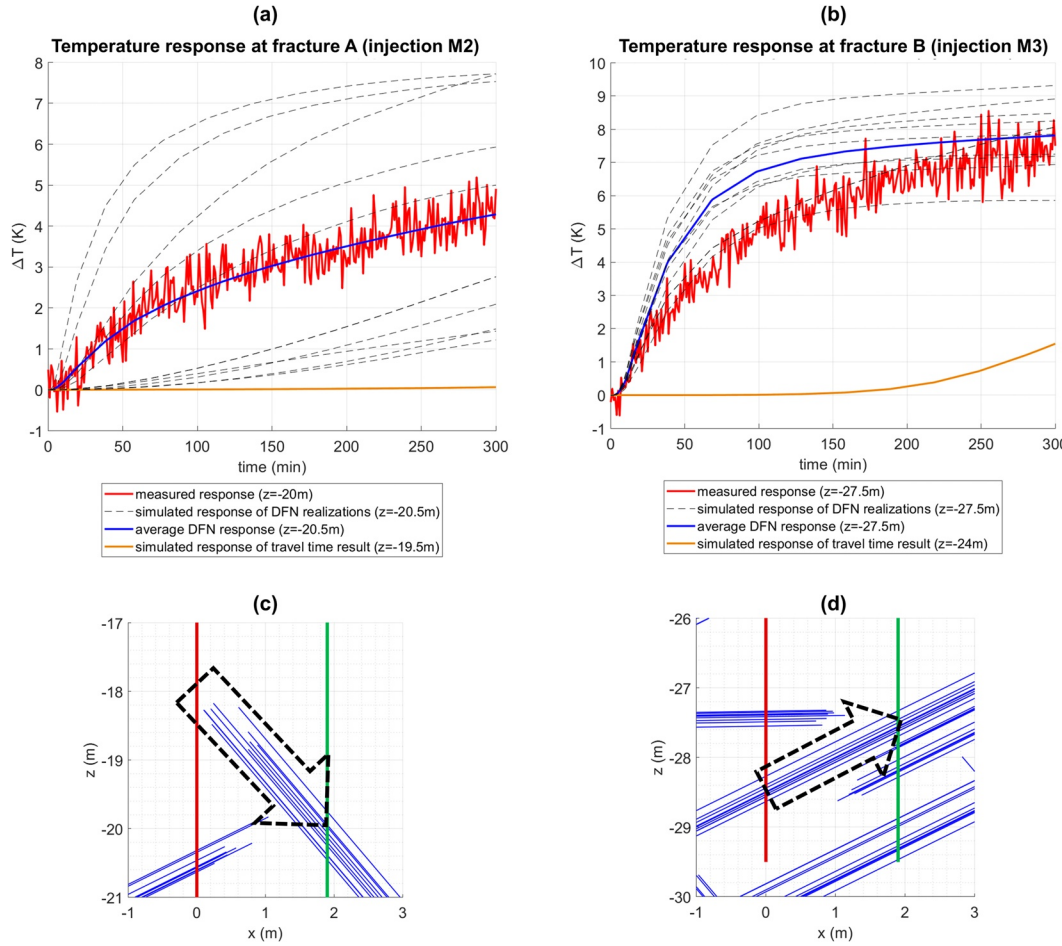

Figure 8. (a) Measured and (b) simulated temperature response curves for fractures A and B. The curves are always generated for the depth showing the greatest temperature amplitude, so that smaller inaccuracies regarding the location of the fractures in the inversion result are not considered in these plots. The plots (c and d) show the 10 individual realizations of the posterior ensemble used for the numerical simulations (blue lines). Here, the black arrows indicate the general direction of heat transport from the injection to the observation borehole.

The simulated temperature data using the continuum-based inversion result (middle column in Figure 7) only reveal one significant temperature anomaly for injection M3 at a depth of −24 m. This corresponds with the high-diffusivity zone observed in the travel time inversion result shown in Figure 2c. As described earlier, the exact depth of this zone cannot be expected to be reproduced by the travel time inversion. Therefore, this high-diffusivity zone can be assumed to resemble fracture B and so we show both thermal responses together in Figure 8b. Compared to the measured data, the response from the travel time inversion result (orange line) is delayed and has a significantly smaller amplitude. We therefore conclude that, although the continuum-based approach actually reproduces this fracture, the estimation of its depth and permeability is not very accurate. At the approximate position of fracture A (Figure 8a), only a very small temperature anomaly is simulated assuming a continuum (which would probably be below the noise level in a field experiment). In this case, the continuum model is not able to correctly predict the heat transport by this fracture.

The simulated temperature data using the hybrid DFN inversion result (right column in Figure 7) is able to reproduce both fractures A and B. The calculated depths of the temperature anomalies are very accurate in comparison with the measured data. There is actually another weak anomaly caused by a fracture in the hybrid DFN result for injection interval M4 at a depth of −37 m. A similar anomaly is also visible in the measured data, but the signal is superimposed by noise and the borehole effects, which hampers reliable interpretation.

When looking at the time dependency as well as the amplitude of the temperature response (Figure 8), it is crucial to distinguish between the individual realizations (shown as black, dashed lines) and the average of those

10 realizations (blue, solid line). For fracture A, a strong variability among the individual realizations can be observed, with maximum temperature deviations ranging from 1 K to almost 8 K at the last time step. The reason is illustrated in Figure 8c, where all 10 DFN realizations are shown as blue lines. The major pathway of heat transport (black arrow) is maintained by a fracture that, although crossing the observation borehole (green line) directly, has no immediate contact to the injection borehole (red line). In the remaining gap, heat is only transported through the rock matrix, which is much slower compared to the heat transport in the fractures. Therefore, besides the exact parameter values assigned to the matrix in the model, the size of the remaining gap (=the distance of the heat transport through the matrix) has a huge impact on the temperature response observed in the other borehole. Since the position of this fracture is adapted and changes during the inversion process, the individual realizations produce strongly differing temperature responses. However, when computing the average of these realizations, the measured data can be predicted almost perfectly. This again highlights the importance of considering the stochastic nature of the hybrid DFN inversion results, as well as the need to model the flow in both discrete fractures and porous matrix within the hybrid DFN approach.

For fracture B, the individual realizations produce more similar temperature responses compared to fracture A, with maximum temperature deviations between 6 and 9 K (Figure 8b). In this case, the fracture directly connects the injection interval with the observation borehole (Figure 8d), so that small variations in the position do not have a strong impact on the heat transport. However, changes in the permeability of the fracture may still affect the results. Again, the prediction of the measured data using the average of 10 DFN realizations is fairly good, even if the rise in temperature is too rapid at early times. For both fractures, the prediction quality using the hybrid DFN inversion result is significantly better than using the continuum model.

5. Discussion

While the main focus of this study is the application of the novel hybrid DFN inversion approach to HT field data, we also want to give a detailed comparison with the continuum-based travel time inversion as well as provide guidance for future applications about how to select the more suitable inversion method under certain conditions.

The main advantage of a continuum-based travel time inversion is the computational efficiency, with a total run time of 15–20 s on a standard laptop for the inversion performed on the HT data set of this study. It also requires less assumptions (and therefore minor a priori knowledge) about certain site conditions, since no boundary conditions have to be defined in the forward model and a lot of details about the experiment (pumping rate, pumping duration, borehole effects) are irrelevant. Despite all those simplifications, the inversion can yield good results for porous media with mostly continuous heterogeneities and allows to identify the major highly transmissive zones within the aquifer. Since the result of the inversion is deterministic, the interpretation of the tomogram is straightforward and does not require any stochastic evaluation.

However, only the diffusivity distribution can be retrieved by the travel time inversion. The conversion to hydraulic conductivity (or permeability) requires information about the specific storage, which can be approximated by a constant value derived from hydraulic attenuation inversion or by further post-processing (Hu et al., 2011; Jiménez et al., 2013). It is also important to note that regularization parameters (e.g., smoothness constraints) may strongly affect the results, and a trial-and-error strategy is often required to find reasonable values for those parameters. Furthermore, although the inversion itself is rather quick, the denoising procedures and picking of the exact travel time can be challenging and time-demanding. The strong simplifications made within the forward model also do not allow an evaluation of the uncertainties of the result.

For the data set of this study, only one out of two high-diffusivity zones (that were clearly visible in the thermal tracer test data) could be identified by the travel time inversion, and inaccuracies were observed in the predicted temperatures as well as in the location of the thermal breakthrough. It is an inherent limitation of the travel time inversion approach in combination with this specific field setup that the exact depth of these highly permeable zones cannot be inferred. Generally, the setup of this hydraulic tomography experiment with a small distance between the two boreholes (1.9 m), but a large vertical extension of the intervals (6 m) is not particularly favorable for performing a travel time inversion. Furthermore, the results indicate that flow between the boreholes is mainly established by narrow zones of high permeability, which might be regarded as fractures. Therefore, a continuum-based inversion approach is probably not suitable to accurately infer the hydraulic properties at this site.

Furthermore, a classical DFN inversion only considering individual fractures, but neglecting the influence of the matrix completely, could not fit the measured data with reasonable quality. Instead, the hybrid DFN inversion produced the best results by accounting for flow in both the matrix and the fractures. We could show that both of the highly transmissive zones could be identified by the hybrid DFN inversion, so that the thermal tracer test data were reproduced very accurately in terms of both location and amplitude of the temperature breakthrough. We therefore conclude that the hybrid DFN results are indeed suitable to be used for flow and transport modeling. Another advantage of the approach is that no preprocessing of the HT data is necessary. Noisy data can be used directly, and the underlying uncertainties are considered in the Bayesian inversion framework. The stochastic nature of the approach allows for the evaluation its uncertainties, for example, in terms of a fracture probability map.

However, a DFN inversion is computationally expensive and may require a high-performance workstation. For the inversion performed for this study, we used a standard desktop PC with an 8-core i7-9700K 3.6 GHz processor and 32 GB RAM. With this setup, a total run time of 4–5 days was required to compute a probabilistic inversion result with a sufficiently large posterior ensemble. The forward model also requires the implementation of appropriate boundary conditions and some assumptions for fractures (e.g., orientation angles of fracture sets, as well as constant aperture and permeability for an individual fracture) are necessary. Therefore, a relatively large amount of a priori knowledge about certain site conditions is crucial to obtain accurate inversion results. It shall also be noted that, although matrix flow is contained in the hybrid DFN model, the matrix parameters are so far assumed constant and need to be predefined, and selecting reasonable values can be a crucial but challenging task. 3D and borehole effects are also neglected (or contained in matrix values) in the current study but could be included for other sites if necessary. Furthermore, due to the stochastic nature of the inversion, the results cannot be interpreted or used for flow and transport modeling directly, but require special post-processing.

We therefore suggest that the decision for one of the inversion approaches should be based on the actual site conditions as well as the expectations about the result. If the data were acquired in a fractured-porous environment with a big contrast in permeability between the rock matrix and individual fractures, the hybrid DFN approach is highly suggested. This was also shown by Fischer et al. (2020) for a karstic and fractured aquifer, where the inferred transmissivities of fracture and matrix differ by several orders of magnitude. However, for an almost impermeable rock matrix (e.g., in most crystalline rocks), where hydraulic connections are exclusively maintained by the fractures, the classical DFN inversion (without matrix flow) can be sufficient (Ringel et al., 2021, 2022). If, on the other hand, the permeability contrast between matrix and fractures is very small, for example, due to only partially open fractures or high fracture surface roughness, the heterogeneities can be assumed continuous, so that the travel time inversion is advantageous due to its simplicity and computational efficiency.

6. Conclusions and Outlook

We have shown that a hybrid DFN inversion approach, considering flow in both discrete fractures and a permeable matrix, is valuable for the hydraulic characterization of fractured-porous sites. The method was successfully applied to HT data acquired at a field site in Göttingen (Germany). For this specific field case, a good fitting of the experimental data could not be achieved by implementing a DFN inversion alone, but only by including a non-zero matrix permeability in the forward model. The results are in general agreement with a standard continuum-based travel time inversion, but the hybrid DFN approach can reveal some hydraulic connectivities in the aquifer with more detail and accuracy. This is also supported by independent validation data, that is, a thermal tracer test conducted at the same site. Here, the inferred DFN ensemble is able to predict the thermal responses with high accuracy regarding the depth, the amplitude, and the time-dependent behavior of the temperature anomalies. However, it is crucial to take the stochastic nature of the approach into account to achieve good results.

The inversion approach might be used for a variety of applications, including the characterization of geothermal sites. For instance, according to a sensitivity study by Heldt et al. (2023), the thermal performance of a high-temperature aquifer thermal energy storage (HT-ATES) system is most sensitive to hydraulic conductivity and its vertical-to-horizontal anisotropy ratio. A preliminary characterization of the aquifer heterogeneity is thus necessary for a better system design and for improving the heat recovery during the operation phase. This characterization should include an accurate representation of both the fracture network and the porous rock matrix (Fischer et al., 2020).

However, this study should only be regarded as a first attempt for including matrix flow within a DFN inversion approach. For future applications of the hybrid DFN inversion, a more generalized procedure can be desirable that has the ability to treat the matrix characteristics (K and S_s) as inversion parameters, and not pre-define them manually. Improvements could also be achieved by implementing spatially variable matrix parameters as well as including borehole effects directly in the forward model. An improved proposal distribution could be generated by considering complementary data (e.g., from geophysical methods) for the generation of DFNs. Furthermore, a proposal distribution could be implemented that considers the correlation between certain parameters, so that more proposed DFNs are likely to be accepted. This would ultimately result in higher computational efficiency. Further research topics include the application of the inversion approach in 3D, as well as the investigation of the resolution and reliability of the hybrid DFN inversion results for cases where only one borehole is available (geothermal applications). For this purpose, preliminary synthetic studies should be conducted to test and improve the methodology, but ultimately more field examples are needed to prove the robustness of the inversion approach.

Data Availability Statement

The experimental data used in this study (hydraulic tomography and thermal tracer test) can be found under the following link: https://doi.org/10.5281/zenodo.10213883.

Acknowledgments
Linwei Hu acknowledges funding and support by Christian Albrechts University Kiel. We thank Jeremy Patterson and two anonymous reviewers for their constructive comments that helped to improve the manuscript and Ryan Pearson for proofreading. Open Access funding enabled and organized by Projekt DEAL.

References

Attard, G., Bayer, P., Rossier, Y., Blum, P., & Eisenlohr, L. (2020). A novel concept for managing thermal interference between geothermal systems in cities. *Renewable Energy*, *145*, 914–924. https://doi.org/10.1016/j.renene.2019.06.095

Baetzel, K. (2017). Hydrogeological characterization of a fractured aquifer based on modelling and heat tracer experiments. (Unpublished master's thesis). University of Göttingen.

Bauer, J. F., Krumbholz, M., Meier, S., & Tanner, D. C. (2017). Predictability of properties of a fractured geothermal reservoir: The opportunities and limitations of an outcrop analogue study. *Geothermal Energy*, *5*(1), 24. https://doi.org/10.1186/s40517-017-0081-0

Berg, S. J., & Illman, W. A. (2011). Three-dimensional transient hydraulic tomography in a highly heterogeneous glaciofluvial aquifer-aquitard system. *Water Resources Research*, *47*(10), W10507. https://doi.org/10.1029/2011wr010616

Berre, I., Doster, F., & Keilegavlen, E. (2019). Flow in fractured porous media: A review of conceptual models and discretization approaches. *Transport in Porous Media*, *130*(1), 215–236. https://doi.org/10.1007/s11242-018-1171-6

Bing, Z., & Greenhalgh, S. A. (2000). Cross-hole resistivity tomography using different electrode configurations. *Geophysical Prospecting*, *48*(5), 887–912. https://doi.org/10.1046/j.1365-2478.2000.00220.x

Binley, A., & Slater, L. D. (2020). *Resistivity and induced polarization—Theory and applications to the near-surface Earth*. Cambridge University Press. https://doi.org/10.1017/9781108685955

Boersma, Q. D., Bruna, P. O., de Hoop, S., Vinci, F., Moradi Tehrani, A., & Bertotti, G. (2021). The impact of natural fractures on heat extraction from tight Triassic sandstones in the West Netherlands Basin: A case study combining well, seismic and numerical data. *Netherlands Journal of Geosciences*, *100*, E6. https://doi.org/10.1017/njg.2020.21

Brauchler, R., Hu, R., Dietrich, P., & Sauter, M. (2011). A field assessment of high-resolution aquifer characterization based on hydraulic travel time and hydraulic attenuation tomography. *Water Resources Research*, *47*(3), W03503. https://doi.org/10.1029/2010WR00963

Brauchler, R., Hu, R., Hu, L., Jiménez, S., Bayer, P., Dietrich, P., & Ptak, T. (2013). Rapid field application of hydraulic tomography for resolving aquifer heterogeneity in unconsolidated sediments. *Water Resources Research*, *49*(4), 2013–2024. https://doi.org/10.1002/wrcr.20181

Brauchler, R., Liedl, R., & Dietrich, P. (2003). A travel time based hydraulic tomographic approach. *Water Resources Research*, *39*(12), 1370. https://doi.org/10.1029/2003wr002262

Bregman, N. D., Bailey, R. C., & Chapman, C. H. (1989). Crosshole seismic tomography. *Geophysics*, *54*(2), 200–215. https://doi.org/10.1190/1.1442644

Cardiff, M., Barrash, W., & Kitanidis, P. K. (2013). Hydraulic conductivity imaging from 3-D transient hydraulic tomography at several pumping/observation densities. *Water Resources Research*, *49*(11), 7311–7326. https://doi.org/10.1002/wrcr.20519

Cardiff, M., Zhou, Y., Barrash, W., & Kitanidis, P. K. (2019). Aquifer imaging with oscillatory hydraulic tomography: Application at the field scale. *Groundwater*, *58*(5), 710–722. https://doi.org/10.1111/gwat.12960

Comsol (1998). Introduction to comsol multiphysics ®.

Day-Lewis, F. D., Slater, L. D., Robinson, J., Johnson, C. D., Terry, N., & Werkema, D. (2017). An overview of geophysical technologies appropriate for characterization and monitoring at fractured-rock sites. *Journal of Environmental Management*, *204*, 709–720. https://doi.org/10.1016/j.jenvman.2017.04.033

Dijkstra, E. W. (1959). A note on two problems in connexion with graphs. *Numerische Mathematik*, *1*(1), 269–271. https://doi.org/10.1007/bf01386390

Fischer, P., Jardani, A., & Jourde, H. (2020). Hydraulic tomography in coupled discrete-continuum concept to image hydraulic properties of a fractured and karstified aquifer (Lez aquifer, France). *Advances in Water Resources*, *137*, 103523. https://doi.org/10.1016/j.advwatres.2020.103523

Fischer, P., Jardani, A., Wang, X., Jourde, H., & Lecoq, N. (2017). Identifying flow networks in a karstified aquifer by application of the cellular automata–based deterministic inversion method (Lez aquifer, France). *Water Resources Research*, *53*(12), 10508–10522. https://doi.org/10.1002/2017wr020921

Gasanzade, F., Pfeiffer, W. T., Witte, F., Tuschy, I., & Bauer, S. (2021). Subsurface renewable energy storage capacity for hydrogen, methane and compressed air—A performance assessment study from the North German Basin. *Renewable and Sustainable Energy Reviews*, *149*, 111422. https://doi.org/10.1016/j.rser.2021.111422

Geuzaine, C., & Remacle, J.-F. (2009). Gmsh: A 3-D finite element mesh generator with built-in pre- and post-processing facilities. *International Journal for Numerical Methods in Engineering*, *79*(11), 1309–1331. https://doi.org/10.1002/nme.2579

Green, P. J. (1995). Reversible jump Markov chain Monte Carlo computation and Bayesian model determination. *Biometrika*, *82*(4), 711–732. https://doi.org/10.1093/biomet/82.4.711

Günther, T., Rücker, C., & Spitzer, K. (2006). Three-dimensional modelling and inversion of DC resistivity data incorporating topography—II. inversion. *Geophysical Journal International*, *166*(2), 506–517. https://doi.org/10.1111/j.1365-246X.2006.03011.x

Heldt, S., Wang, B., & Bauer, S. (2023). Parameter identification and range restriction through sensitivity analysis for a high-temperature heat injection test. *Geothermal Energy*, *11*(1), 12. https://doi.org/10.1186/s40517-023-00255-5

Hou, X., Hu, R., Yeh, T.-C. J., Li, Y., Qi, J., Song, Y., & Qiu, H. (2023). A short-term pumping strategy for hydraulic tomography based on the successive linear estimator. *Water Resources Research*, *59*(4), e2022WR033831. https://doi.org/10.1029/2022WR033831

Hu, R., Brauchler, R., Herold, M., & Bayer, P. (2011). Hydraulic tomography analog outcrop study: Combining travel time and steady shape inversion. *Journal of Hydrology*, *409*(1–2), 350–362. https://doi.org/10.1016/j.jhydrol.2011.08.031

Huang, Y., Pang, Z., Kong, Y., & Watanabe, N. (2021). Assessment of the high-temperature aquifer thermal energy storage (HT-ATES) potential in naturally fractured geothermal reservoirs with a stochastic discrete fracture network model. *Journal of Hydrology*, *603*, 127188. https://doi.org/10.1016/j.jhydrol.2021.127188

Illman, W. A., Liu, X., Takeuchi, S., Jim Yeh, T.-C., Ando, K., & Saegusa, H. (2009). Hydraulic tomography in fractured granite: Mizunami underground research site, Japan. *Water Resources Research*, *45*(1), W01406. https://doi.org/10.1029/2007WR006715

Jiménez, S., Brauchler, R., & Bayer, P. (2013). A new sequential procedure for hydraulic tomographic inversion. *Advances in Water Resources*, *62*, 59–70. https://doi.org/10.1016/j.advwatres.2013.10.002

Klepikova, M., Brixel, B., & Jalali, M. (2020). Transient hydraulic tomography approach to characterize main flowpaths and their connectivity in fractured media. *Advances in Water Resources*, *136*, 103500. https://doi.org/10.1016/j.advwatres.2019.103500

Klepikova, M., Le Borgne, T., Bour, O., Gallagher, K., Hochreutener, R., & Lavenant, N. (2014). Passive temperature tomography experiments to characterize transmissivity and connectivity of preferential flow paths in fractured media. *Journal of Hydrology*, *512*, 549–562. https://doi.org/10.1016/j.jhydrol.2014.03.018

Kushnir, A. R. L., Heap, M. J., & Baud, P. (2018). Assessing the role of fractures on the permeability of the Permo-Triassic sandstones at the Soultz-sous-Forêts (France) geothermal site. *Geothermics*, *74*, 181–189. https://doi.org/10.1016/j.geothermics.2018.03.009

Lang, P. S., Paluszny, A., Nejati, M., & Zimmerman, R. W. (2018). Relationship between the orientation of maximum permeability and intermediate principal stress in fractured rocks. *Water Resources Research*, *54*(11), 8734–8755. https://doi.org/10.1029/2018WR023189

Li, H., Lu, C., Werner, A. D., Irvine, D. J., & Luo, J. (2022). Impacts of heterogeneity on aquifer storage and recovery in saline aquifers. *Water Resources Research*, *58*(5), e2021WR031306. https://doi.org/10.1029/2021WR031306

Liu, Q. (2022). Characterization of hydraulic properties in fractured aquifers using slug test-based hydraulic tomography and thermal tracer tomography. Doctoral dissertation. Universität Göttingen. https://doi.org/10.53846/goediss-9495

Liu, Q., Hu, L., Hu, R., Brauchler, R., Xing, Y., Qi, J., & Ptak, T. (2023). Characterization of aquifer heterogeneity by tomographic slug test responses considering wellbore effects. *Journal of Hydrology*, *627*(B), 130472. https://doi.org/10.1016/j.jhydrol.2023.130472

Liu, Q., Hu, R., Hu, L., Xing, Y., Qiu, P., Yang, H., et al. (2022). Investigation of hydraulic properties in fractured aquifers using cross-well travel-time based thermal tracer tomography: Numerical and field experiments. *Journal of Hydrology*, *609*, 127751. https://doi.org/10.1016/j.jhydrol.2022.127751

Luo, N., Zhao, Z., Illman, W. A., Zha, Y., Mok, C. M. W., & Yeh, T.-C. J. (2023). Three–dimensional steady–state hydraulic tomography analysis with integration of cross–hole flowmeter data at a highly heterogeneous site. *Water Resources Research*, *59*(6), e2022WR034034. https://doi.org/10.1029/2022WR034034

Qiu, H., Hu, R., Luo, N., Illman, W. A., & Hou, X. (2023). Comparison of travel-time and geostatistical inversion approaches for hydraulic tomography: Synthetic modeling study on data density and well configuration issues. *Journal of Hydrology*, *618*, 129247. https://doi.org/10.1016/j.jhydrol.2023.129247

Qiu, P. (2020). Automated data processing and numerical methods for travel-time based hydraulic tomography. Doctoral dissertation. Universität Göttingen. https://doi.org/10.53846/goediss-8150

Ren, S., Zhang, Y., Jim Yeh, T.-C., Wang, Y., & Carr, B. J. (2021). Multiscale hydraulic conductivity characterization in a fractured granitic aquifer: The evaluation of scale effect. *Water Resources Research*, *57*(9), e2020WR028482. https://doi.org/10.1029/2020WR028482

Ringel, L. M., Jalali, M., & Bayer, P. (2021). Stochastic inversion of three-dimensional discrete fracture network structure with hydraulic tomography. *Water Resources Research*, *57*(12), e2021WR030401. https://doi.org/10.1029/2021WR030401

Ringel, L. M., Jalali, M., & Bayer, P. (2022). Characterization of the highly fractured zone at the Grimsel Test Site based on hydraulic tomography. *Hydrology and Earth System Sciences*, *26*(24), 6443–6455. https://doi.org/10.5194/hess-26-6443-2022

Ringel, L. M., Somogyvári, M., Jalali, M., & Bayer, P. (2019). Comparison of hydraulic and tracer tomography for discrete fracture network inversion. *Geosciences*, *9*(6), 274. https://doi.org/10.3390/geosciences9060274

Rücker, C., Günther, T., & Wagner, F. M. (2017). pyGIMLi: An open-source library for modelling and inversion in geophysics. *Computers & Geosciences*, *109*, 106–123. https://doi.org/10.1016/j.cageo.2017.07.011

Schön, J. (2015). *Physical properties of rocks—Fundamentals and principles of petrophysics* (2nd ed., Vol. 18). Elsevier.

Somogyvári, M., & Bayer, P. (2017). Field validation of thermal tracer tomography for reconstruction of aquifer heterogeneity. *Water Resources Research*, *53*(6), 5070–5084. https://doi.org/10.1002/2017wr020543

Somogyvári, M., Jalali, M., Parras, S. J., & Bayer, P. (2017). Synthetic fracture network characterization with transdimensional inversion. *Water Resources Research*, *53*(6), 5104–5123. https://doi.org/10.1002/2016WR020293

Somogyvári, M., Kühn, M., & Reich, S. (2019). Reservoir-scale transdimensional fracture network inversion. *Advances in Geosciences*, *49*, 207–214. https://doi.org/10.5194/adgeo-49-207-2019

Song, Y., Hu, R., Liu, Q., Qiu, H., Hou, X., Qi, J., & Konadu-Amoah, B. (2023). Comparison of hydraulic travel time and attenuation inversions, thermal tracer tomography and geostatistical inversion for aquifer characterization: A numerical study. *Water*, *15*(13), 2401. https://doi.org/10.3390/w15132401

Tiedeman, C. R., & Barrash, W. (2020). Hydraulic tomography: 3D hydraulic conductivity, fracture network, and connectivity in mudstone. *Groundwater*, *58*(2), 238–257. https://doi.org/10.1111/gwat.12915

Werner, H. (2013). Strukturgeologische Charakterisierung eines Geothermietestfeldes auf der Basis bohrlochgeophysikalischer Messdaten und Bohrkerngefügen auf dem Göttinger Nordcampus. (Unpublished master's thesis). University of Göttingen.

Woodbury, A., & Zhang, K. (2001). Lanczos method for the solution of groundwater flow in discretely fractured porous media. *Advances in Water Resources*, *24*(6), 621–630. https://doi.org/10.1016/S0309-1708(00)00047-6

Yang, H., Hu, R., Qiu, P., Liu, Q., Xing, Y., Tao, R., & Ptak, T. (2020). Application of wavelet de-noising for travel-time based hydraulic tomography. *Water*, *12*(6), 1533. https://doi.org/10.3390/w12061533

Yeh, T.-C. J., & Liu, S. (2000). Hydraulic tomography: Development of a new aquifer test method. *Water Resources Research*, *36*(8), 2095–2105. https://doi.org/10.1029/2000WR900114

Zha, Y., Yeh, T.-C. J., Illman, W. A., Tanaka, T., Bruines, P., Onoe, H., & Saegusa, H. (2015). What does hydraulic tomography tell us about fractured geological media? A field study and synthetic experiments. *Journal of Hydrology*, *531*, 17–30. https://doi.org/10.1016/j.jhydrol.2015.06.013

Zhao, Z., Illman, W. A., Zha, Y., Yeh, T.-C. J., Mok, C. M. B., Berg, S. J., & Han, D. (2019). Transient hydraulic tomography analysis of fourteen pumping tests at a highly heterogeneous multiple aquifer–aquitard system. *Water*, *11*(9), 1864. https://doi.org/10.3390/w11091864

Zhao, Z., Luo, N., & Illman, W. A. (2023). Geostatistical analysis of high-resolution hydraulic conductivity estimates from the hydraulic profiling tool and integration with hydraulic tomography at a highly heterogeneous field site. *Journal of Hydrology*, *617*, 129060. https://doi.org/10.1016/j.jhydrol.2023.129060